

Interfaces between MoOx and MoX2 (X=S, Se, and Te)

Fengming Chen(陈凤鸣), Jinxin Liu(刘金鑫), Xiaoming Zheng(郑晓明), Longhui Liu(刘龙慧), Haipeng Xie(谢海鹏), Fei Song(宋飞), Yongli Gao(高永立), Han Huang(黄寒)

Citation: Chin. Phys. B . 2020, 29 (**11**): 116802. **doi:** 10.1088/1674-1056/abb310
Journal homepage: http://cpb.iphy.ac.cn; http://iopscience.iop.org/cpb

What follows is a list of articles you may be interested in

Covalent coupling of DNA bases with graphene nanoribbon electrodes:Negative differential resistance, rectifying, and thermoelectric performance

Peng-Peng Zhang(张鹏鹏), Shi-Hua Tan(谭仕华), Xiao-Fang Peng(彭小芳), Meng-Qiu Long(龙孟秋)

Chin. Phys. B . 2020, 29(10): 106801 . **doi:** 10.1088/1674-1056/aba9bf

Selective linear etching of monolayer black phosphorus using electron beams

Yuhao Pan(潘宇浩), Bao Lei(雷宝), Jingsi Qiao(乔婧思), Zhixin Hu(胡智鑫), Wu Zhou(周武), Wei Ji(季威)

Chin. Phys. B . 2020, 29(8): 086801 . **doi:** 10.1088/1674-1056/ab9438

Scalable preparation of water-soluble ink of few-layered WSe_2 nanosheets for large-area electronics

Guoyu Xian(冼国裕), Jianshuo Zhang(张建烁), Li Liu(刘丽), Jun Zhou(周俊), Hongtao Liu(刘洪涛), Lihong Bao(鲍丽宏), Chengmin Shen(申承民), Yongfeng Li(李永峰), Zhihui Qin(秦志辉), Haitao Yang(杨海涛)

Chin. Phys. B . 2020, 29(6): 066802 . **doi:** 10.1088/1674-1056/ab889e

Effect of initial crystallization temperature and surface diffusion on formation of GaAs multiple concentric nanoring structures by droplet epitaxy

Yi Wang(王一), Xiang Guo(郭祥), Jiemin Wei(魏节敏), Chen Yang(杨晨), Zijiang Luo(罗子江), Jihong Wang(王继红), Zhao Ding(丁召)

Chin. Phys. B . 2020, 29(4): 046801 . **doi:** 10.1088/1674-1056/ab790b

Surface effects on the thermal conductivity of silicon nanowires

Hai-Peng Li(李海鹏), Rui-Qin Zhang(张瑞勤)

Chin. Phys. B . 2018, 27(3): 036801 . **doi:** 10.1088/1674-1056/27/3/036801

REVIEW

Interfaces between MoO_x and MoX_2 (X = S, Se, and Te)*

Fengming Chen(陈凤鸣)[1], Jinxin Liu(刘金鑫)[1], Xiaoming Zheng(郑晓明)[1], Longhui Liu(刘龙慧)[1], Haipeng Xie(谢海鹏)[1], Fei Song(宋飞)[2], Yongli Gao(高永立)[3,1], and Han Huang(黄寒)[1,†]

[1] Hunan Key Laboratory of Super-microstructure and Ultrafast Process, School of Physics and Electronics, Central South University, Changsha 410083, China
[2] Shanghai Synchrotron Radiation Facility, Shanghai Institute of Applied Physics, Chinese Academy of Sciences, Shanghai 201204, China
[3] Department of Physics and Astronomy, University of Rochester, Rochester, NY 14627, USA

(Received 8 July 2020; revised manuscript received 10 August 2020; accepted manuscript online 27 August 2020)

In the past decades there have been many breakthroughs in low-dimensional materials, especially in two-dimensional (2D) atomically thin crystals like graphene. As structural analogues of graphene but with a sizeable band gap, monolayers of atomically thin transition metal dichalcogenides (with formula of MX_2, M = Mo, W; X = S, Se, Te, etc.) have emerged as the ideal 2D prototypes for exploring fundamentals in physics such as valleytronics due to the quantum confinement effects, and for engineering a wide range of nanoelectronic, optoelectronic, and photocatalytic applications. Transition metal trioxides as promising materials with low evaporation temperature, high work function, and inertness to air have been widely used in the fabrication and modification of MX_2. In this review, we reported the fabrications of one-dimensional MoS_2 wrapped MoO_2 single crystals with varied crystal direction via atmospheric pressure chemical vapor deposition method and of 2D MoO_x covered MoX_2 by means of exposing MoX_2 to ultraviolet ozone. The prototype devices show good performances. The approaches are common to other transition metal dichalcogenides and transition metal oxides.

Keywords: MoO_x, epitaxial relationships, MoX_2, layer-by-layer oxidation

PACS: 68.65.–k, 73.90.+f, 82.80.Pv, 79.60.Jv **DOI:** 10.1088/1674-1056/abb310

1. Introduction

Advanced materials play important roles in our daily lives. Since the 1980s, dimensionality has been an important subject in the fields of condensed matter physics and materials sciences. Due to their exceptional electrical, thermal, and optical properties originating from the quantum confinement effects, low-dimensional materials are promising for applications in nanoelectronic devices, energy storage, energy conversion, and thermal management.[1–3] It is possible to precisely tune the materials' properties at atomic level. Graphene a "superstar" of two-dimensional (2D) atomically thin crystals with exotic electronic, optical and mechanical properties[4–6] is promoting extensive researches on other 2D materials,[7,8] including hexagonal boron nitride,[9,10] transition metal dichalcogenides (TMDCs),[11,12] black phosphene,[13–15] silicene,[16,17] germanene,[18,19] and so on.

A significant advance in the 2D atomically thin crystal field is the rediscovery of TMDCs in the past decade,[20–22] which have long been used as industrial solid state lubricants. It has been largely driven by the increasing research interests in group-VIB metal dichalcogenides (with formula of MX_2, M = Mo, W; X = S, Se, Te) with sizable bandgaps of 1–2 eV.[23] which ensures the high on/off current ratio and the direct band gap emissions.[24] The constituent layers in MX_2 are covalently bonded in the 2D plane, but weakly coupled with neighboring layers through van der Waals (vdW) interactions. Figure 1(a) shows the typical atomic structure of monolayer molybdenum disulfide (MoS_2), which consists of a layer of Mo atoms sandwiched between two layers of S atoms. Each Mo atom is connected to six S atoms covalently. MoS_2 belongs to the hexagonal crystal system. Monolayer MoS_2 is advantageous for the development of optoelectronic devices because it has a direct band gap of $\sim$ 1.8 eV, in contrast to the bulk MoS_2, which has an indirect band gap of 1.3 eV. Monolayer MoS_2 has a charge carrier mobility up to 200 $cm^2 \cdot V^{-1} \cdot s^{-1}$ and a current on/off ratio of 1×10^8 at room temperature with hafnium oxide as gate dielectric.[25–28] The excellent performances prove TMDC to be potential substitutes of Si in conventional electronics and of organic semiconductors in wearable and flexible systems.[13,29–31]

Among the methods to grow ultrathin TMDCs,[32–37] chemical vapor deposition (CVD) is a most promising one with large-area and high quality. However, many TMDCs (such as M = Nb, Pt, Ti) are very difficult to be synthesized due to the high melting temperatures and low vapor pressure. The synergistic additive-assisted methods including salt assistance, gas assistance, and template assistance are introduced

*Project supported by the National Natural Science Foundation of China (Grant No. 11874427), the National Science Foundation DMR-1903962, and the Fundamental Research Funds for the Central Universities of Central South University (Grant No. 2019zzts429).

†Corresponding author. E-mail: physhh@csu.edu.cn

© 2020 Chinese Physical Society and IOP Publishing Ltd

to solve this problem.[38] Among them, the alkali-metal assistance method (for example, NaCl and KCl) is of great importance and 47 compounds and heterostructures have been synthesized at moderate condition.[39] In order to realize full potential for practical application, many efforts have been devoted to the development of methods to wafer-scale 2D materials. For example, 4-inch wafer-scale MoS_2 films with high-mobility and excellent spatial homogeneity have been CVD grown directly on SiO_2.[40] Furthermore, TMDC heterostructures such as MoS_2–WS_2 and $MoSe_2$–WS_2 have been grown via CVD method, offering a new opportunity to explore novel physics and 2D devices for optoelectronics and light harvesting.[41,42]

The controllable methods to tune the properties of 2D MX_2 remain a key challenge with regard to practical application. One kind of ways is reducing the dimensionality further, which leads to many novel properties.[43–49] For example, graphene transforms from semimetal to semiconductor when narrowing to one-dimensional (1D) nanoribbons.[50] Up to now, there are several methods to synthesize graphene nanoribbons, including topdown lithography,[7,50] unzipping carbon nanotube[44,45,51] and bottomup on surface syntheses,[52–56] and so on. However, 1D MoS_2 has less stability and has been less studied.[57] It is theoretically predicted that 1D zigzag-edged MoS_2 nanoribbons are metallic and exhibit unusual magnetic properties. The magnetic moment mainly concentrates on the edge atoms.[58] In addition, the armchair-edged MoS_2 nanobelts with width down to 4 nm have a high and robust mobility comparable to its 2D sheet counterpart.[59] Metastable 1D MoS_2 nanoribbons with metallic and ferromagnetic properties were synthesized by the sulfurization of MoO_3 nanoribbons.[57] Metallic MoS_2 nanoribbons less than 1 nm in width have been directly fabricated in a MoS_2 monolayer by using focused-electron-beam-based techniques, although severe mechanical deformations occurred.[60] Recently, monolayer MoS_2 nanoribbons in a width of few tens to thousands of nanometers have been grown on NaCl or monolayer MoS_2 via a NaCl assisted vapor-liquid-solid method.[46] It is still a challenge for the preparation of 1D MoS_2 nanoribbons.

The other kind of ways is surface charge transfer doping via the interfaces between 2D layers and *in-situ* thermally evaporated materials with either high or low work functions (WF) under high vacuum condition.[61] Cesium carbonate (Cs_2CO_3) with a low WF of 1.9–2.2 eV is an n-dopant.[62] MoS_2 FETs with thermally-evaporated Cs_2CO_3 cover layer possess good stability and increased electron mobility.[63] The same is true for WSe_2, where the electron mobility is increased from 3.9 $cm^2 \cdot V^{-1} \cdot s^{-1}$ to 27 $cm^2 \cdot V^{-1} \cdot s^{-1}$ and the photoresponsivity is increased by almost three orders of magnitude from 0.92 $A \cdot W^{-1}$ to 575 $A \cdot W^{-1}$.[64] Furthermore, the transition from p- to n-type semiconductor for BP is demonstrated upon thermally depositing 10 nm Cs_2CO_3 on top, where the electron mobility of BP is significantly increased from 1.1 $cm^2 \cdot V^{-1} \cdot s^{-1}$ to $\sim$ 27 $cm^2 \cdot V^{-1} \cdot s^{-1}$.[65] Transition metal trioxides (i.e., WO_3, MoO_3) with high WF are p-dopants, which can not only strongly p-dope graphene and lower the sheet resistance,[66,67] but also allow for an efficient hole-injection for organic devices and organic–inorganic hybrid perovskite solar cells.[68–72] Intense hole transfer from MoO_x side to CuPc side has been demonstrated.[73] The organic FETs having Au/MoO_3 electrodes exhibit on average 33 smaller contact resistance values than the device having bare Au electrodes at the gate voltage of -6 V.[74] Upon thermally depositing MoO_3, the WSe_2 FET is tuned from ambipolar to p-type and the on/off ratios increase from 10^3 to 10^4.[75] However, the thermally deposited films have drawbacks such as poor control of thickness and uniformity.[75,76] In the controlled conditions such as oxygen plasma or ultraviolet ozone (UVO), a dense oxide layer can be formed immediately.[77,78]

MoO_3 as promising materials with a low evaporation temperature, a high WF up to 6.3 eV, and inertness to air have been widely used in the fabrication and modification of MX_2. It can be reduced into metallic MoO_2 crystals, whose atomic structure is shown in Fig. 1(b). In this review we report our recent progress on MoO_2@MoS_2 nanorods and UVO treated MoX_2 flakes, which are common to other MX_2. This review consists of following two sections: 1. 1D MoO_2@MoS_2 nanorods. 1D MoS_2 wrapped MoO_2 single crystals with varied crystal direction are synthesized via atmospheric pressure chemical vapor deposition (APCVD) method.[79,80] Devices based on individual transferred MoO_2@MoS_2 nanorods show high conductivity and the contact resistance was calculated to be three orders of magnitude less than previous reported one.[81] Based on the MoO_2@MoS_2 core–shell structure, a facile approach is developed to single- and bi-layered MoS_2 nanoribbons by PMMA assisted decoupling.[82] 1D MoS_2 nanoribbons can also be synthesized via a CVD method without catalysts.[83] 2. 2D MoO_x/MoX_2 heterojunction. We report the layer-by-layer oxidation of atomically thin MoX_2 (X = Se, Te) flakes into MoO_x via UVO, as shown in Fig. 1(c), and demonstrate the p-doping effect of MoO_x on the remained few-layered MoX_2 (X = Se, Te),[84–86] as revealed by photoelectron spectroscopy (PES),[87,88] Raman, and PL, as well as transport measurements. The excellent performances of MoO_x/MoX_2 devices can be ascribed to the surface charge transfer induced p-doping of MoX_2 and the inertness of the dense MoO_x capping layer.

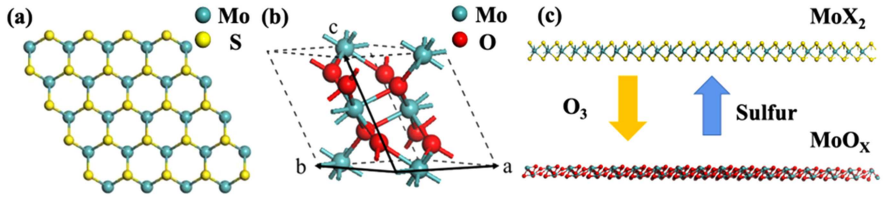


Fig. 1. Crystal structures of MoS_2 (a) and MoO_2 (b). (c) Schematic of transition between MoO_x and MoX_2.

2. 1D MoO_2@MoS_2 nanorods

Recently, MoO_2 core–shell nanostructured materials, i.e., MoO_2@MoS_2, have gained much interests due to their excellent properties and various applications.[89,90] The capability of modifying and tuning the properties of these core–shell nanomaterials enables them to be utilized in a range of applications such as light-emitting diodes,[91] optical concentrators,[92] electronic and photonic devices,[93] etc. Various methods are used to synthesis MoO_2 nanostructures on different substrates including Cu,[94] silicon,[95–97] and sapphire (Al_2O_3).[98–101] Herein, we are interested in the three most common crystallographic planes of sapphire which are used as substrates for epitaxial growth. Figures 2(a)–2(c) show the schematic description of the atomic distribution at the surfaces of c-, m-, and a-sapphire. For c-sapphire, the surface shows a periodic hexagon structure formed by aluminum atoms. In the cases of m- and a-sapphire, they exhibit a rectangle periodic structure formed by aluminum atoms or oxygen atoms. The difference in substrate symmetry may result in different structures and properties of epitaxially grown materials.[100]

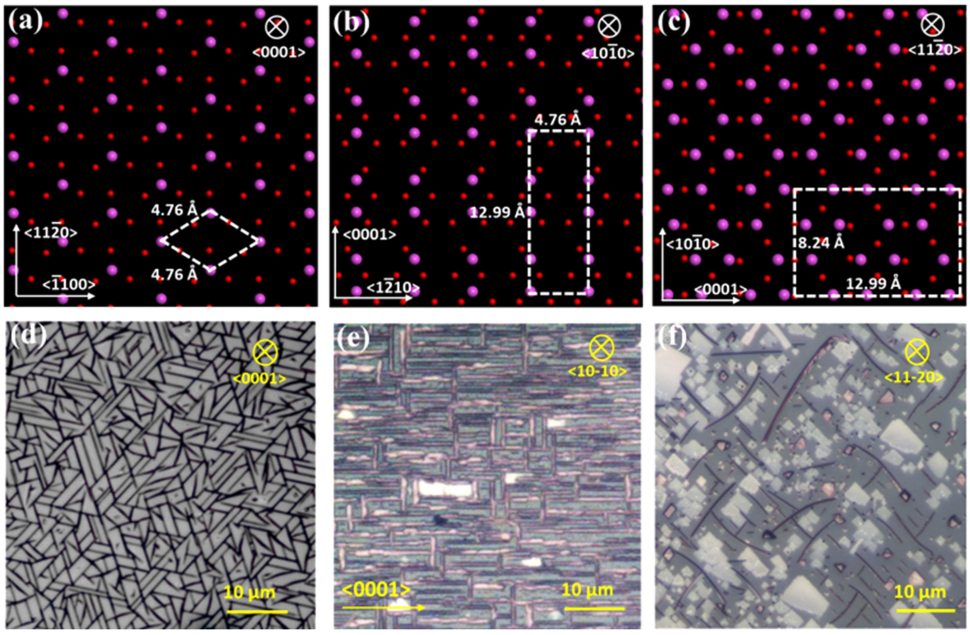


Fig. 2. Morphologies. Schematic description of the crystalline structure at the surfaces of (a) c-sapphire, (b) m-sapphire, and (c) a-sapphire. Al atoms and O atoms are represented by purple and red balls, respectively. The unit cells and lattice constants are marked. The representative OM images of nanorods on (d) c-sapphire, (e) m-sapphire, and (f) a-sapphire.[80]

One-dimensional (1D) single crystals with varied crystal directions are synthesized via APCVD method on them. Figure 2(d) shows a typical OM image of the as-grown nanorods on c-sapphire. Most of them are straight and highly oriented 60° to each other, suggesting a good epitaxial relationship. They are grown along sapphire $\langle 10\bar{1}0\rangle$. As the substrate changes to be m-sapphire, the growth direction of nanorods changes into two directions perpendicular to each other, that is sapphire $\langle 0001\rangle$ and sapphire $\langle 1\bar{2}10\rangle$ (Fig. 2(e)). Nevertheless, when a-sapphire is used (Fig. 2(f)), most of as-made products are square-like while a small number of them are rod-like but curved, indicating that there is no epitaxial relationship. Taking the main crystallographic directions of c-, m-, and a-sapphire ($\langle 10\bar{1}0\rangle$ vs. $\langle 1\bar{2}10\rangle$, $\langle 0001\rangle$ vs. $\langle 1\bar{2}10\rangle$, and $\langle 10\bar{1}0\rangle$ vs. $\langle 0001\rangle$) into account, we conclude that the nanorods have less preference to grow along the sapphire $\langle 1\bar{2}10\rangle$ direction. On a-sapphire, the curved topography of the nanorods is subject to the competition in the epitaxial growth along $\langle 10\bar{1}0\rangle$ and $\langle 0001\rangle$ directions, suggesting the comparative growing barriers in these two directions.

The sulfurization process in the APCVD occurs in two steps, involving the reduction of MoO_3 to MoO_2 in the first step, followed by MoO_2 being converted into MoS_2. Thus, there are three classes of products: MoS_2, MoO_2, and

MoO_2@MoS_2. MoS_2 flakes have triangular shapes and can be easily distinguished in OM images. Raman spectroscopy measurements were performed to characterize the compositions of the nanorods. Figure 3(a) displays the Raman spectra (from top to bottom) of MoS_2 (m-MoS_2), MoO_2@MoS_2nanorods (m-MoO_2@MoS_2 nanorods), MoO_2 nanorods (m-nanorods) on m-sapphire, as well as MoO_2 nanorods (c-nanorods), MoO_2@MoS_2 nanorods (c-MoO_2@MoS_2 nanorods), and MoS_2 (c-MoS_2) on c-sapphire, respectively. Here c- and m- indicate the sapphire surfaces. There are two characteristic peaks for the as-grown MoS_2 flakes located at ~ 385 cm^{-1} and ~ 405 cm^{-1}, corresponding to E^1_{2g} (in-plane) and A_{1g} (out-of-plane) Raman modes, respectively.[102,103] For MoO_2 nanorods, the representative Raman spectra in Fig. 3(a) (magenta solid curve and blue solid curve) show several peaks at 204 cm^{-1}, 227 cm^{-1}, 347 cm^{-1}, 362 cm^{-1}, 459 cm^{-1}, 495 cm^{-1}, 569 cm^{-1}, and 744 cm^{-1}, in good agreement with those for MoO_2 crystals.[104] For MoO_2@MoS_2 nanorods, the Raman spectra (olive solid curve and red solid curve) show the fingerprinting features of both MoS_2 and MoO_2.[105–107]

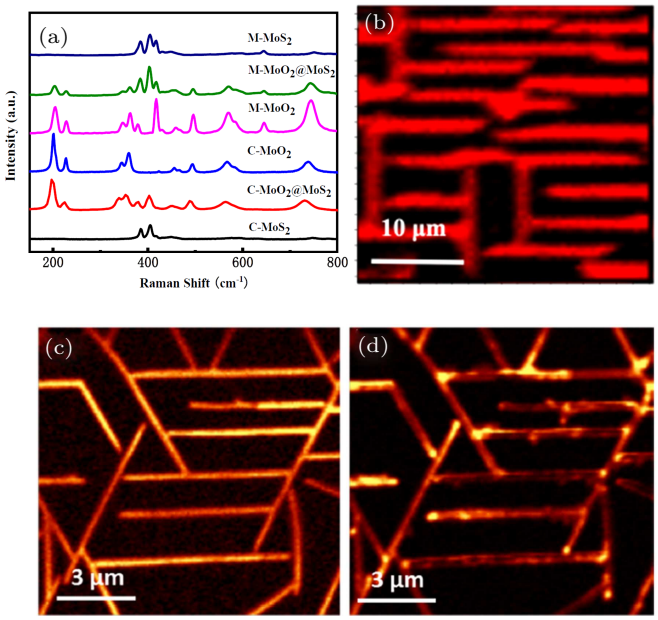


Fig. 3. Compositions. (a) Typical Raman spectra of as-made c- and m-MoO_2@MoS_2 nanorods, nanorods, and MoS_2. (b) Raman map of m-nanorods at 207 cm^{-1}. Raman maps of c-nanorods at (c) 201 cm^{-1} and (d) 400 cm^{-1}.[79,80]

Compared with that for c-MoO_2@MoS_2, a red shift of MoS_2-related Raman A_{1g} peak for m-MoO_2@MoS_2 is recorded as 1.2 cm^{-1}. It can be ascribed to the difference in the interfacial interaction. It is found that c-nanorods are more easily to be sulfurized compared with m-nanorods under the same experimental conditions. The Raman mappings of m-nanorods at 204 cm^{-1} (Fig. 3(b)), c-nanorods at 201 cm^{-1} (Fig. 3(c)) and 400 cm^{-1} (Fig. 3(d)) present highly oriented nanorods with uniform contrast.[108] In the following, for convenience, MoO_2 nanorods are not distinguished from MoO_2@MoS_2 core-shell nanorods when discussing about MoO_2.

Figure 4(a) displays the typical XRD (θ–2θ scan) patterns of the m- (blue) and c-nanorods (black), which display a single phase. The blue XRD pattern displays a sharp diffraction peak at $2\theta = 66.4°$, corresponding to $MoO_2(202)$ (JCPDS No. 32-671). The diffraction peaks at $2\theta = 43.1°$ and $68.3°$ correspond to sapphire $(20\bar{2}0)$ and $(30\bar{3}0)$, respectively.[109] It suggests that the m-nanorods are monoclinic with the orientation relationship of $MoO_2(101)||$sapphire $(10\bar{1}0)$. The black XRD pattern displays an outstanding diffraction peak at $2\theta = 37.1°$, corresponding to $MoO_2(200)$, which is similar to the results in MoO_2 films.[110–112] The sharp peak at $2\theta = 41.9°$ corresponds to sapphire (0006). It suggests that the c-nanorods are monoclinic with the orientation relationship of $MoO_2(100)||$ sapphire (0001).[113] Figure 4(b) shows the corresponding 2D-grazing incidence x-ray diffraction pattern for c-nanorods with the incident plane of c-sapphire $(1\bar{2}10)$. The inset in Fig. 4(b) is the schematic of the measurements. The diffraction maximum marked by the red circle is positioned at $q_z = 13.00$ nm^{-1} and $q_{xy} = 12.65$ nm^{-1}, which could be indexed to an interplane distance of 3.46 Å, and assigned to MoO_2 (110).

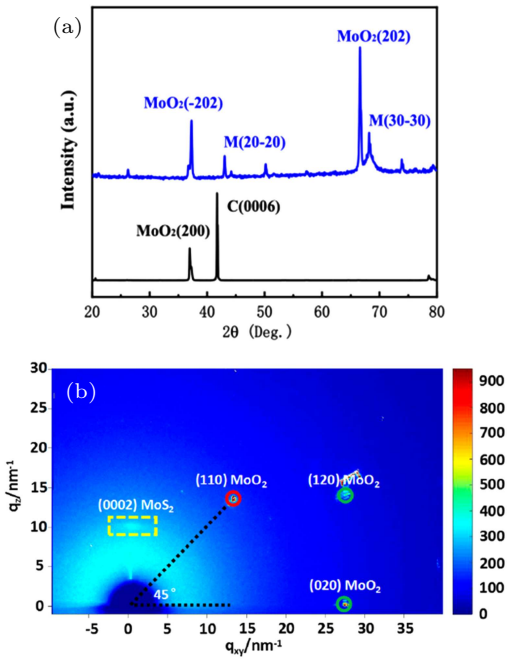


Fig. 4. Global structural properties. (a) XRD patterns of c- (black) and m-nanorods (blue). (b) 2D-GIXRD pattern of c-nanorods.[79]

Figure 5(a) displays the cross sectional SEM image of a single c-nanorod in a shape of isosceles trapezoid with a dihedral angle between sloping side facets and bottom plane of $\sim 45°$. As the substrate is changed to be m-sapphire, the dihedral angle between sloping side facets and bottom plane is $\sim 30°$ (Fig. 5(b)). According to the formula of interfacial angel of monoclinic crystal system and crystallographic

analysis, the sloping side facets of c-nanorod are MoO_2 (110) and MoO_2 ($1\bar{1}0$). For the m-nanorod, the sloping side facets are MoO_2 (001) and MoO_2 (100).[114] The corresponding atomically resolved HRTEM image at the upper-left corner in Fig. 5(c) displays the interplanar spacings of 0.238 nm and 0.276 nm, corresponding to the MoO_2 (020) and MoO_2 ($10\bar{2}$), respectively. This result is consist with the SAED pattern, confirming that these nanorods grow along MoO_2 ⟨100⟩ direction.[115–117] The inset in Fig. 5(d) reveals the superior crystallization of m-nanorods, exhibiting the interplanar spacing values of 0.340 nm and 0.486 nm, in agreement with that of MoO_2 (011) and MoO_2 ($10\bar{1}$), respectively, confirming that these m-nanorods grow along MoO_2 ⟨010⟩ direction. Thus, the crystallographic growth direction of MoO_2 nanorods can be controlled via the change of the substrate. The corresponding EDS spectra of c-nanorod (Fig. 5(e)) and m-nanorod (Fig. 5(f)) reveal that the atomic ratio between O and Mo is 1.97 and 1.96, respectively, indicating pure MoO_2 cores. Conclusively, from c- to m-sapphire, the growth direction of epitaxial MoO_2 nanorods changes from along ⟨001⟩ to ⟨010⟩ of bulk monoclinic MoO_2 accompanied by exposing different surfaces.

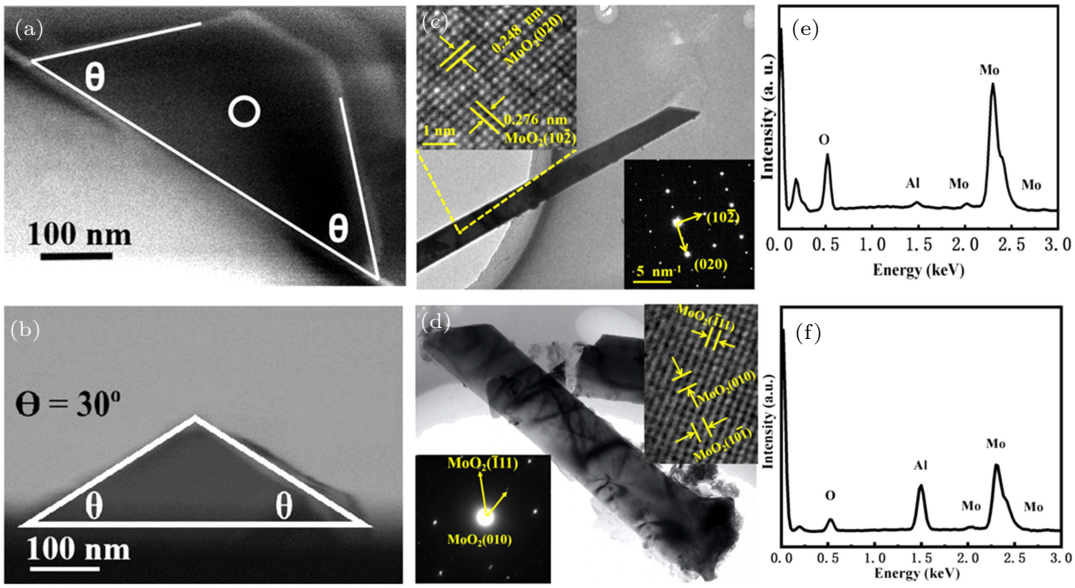


Fig. 5. Local structural properties. Cross-sectional SEM image of single (a) c-nanorod and (b) m-nanorod. (c) Low magnification image of c-nanorod. The insets show the HRTEM image in [201] zone and the corresponding SAED pattern. (d) Low-magnification TEM image of m-nanorod. Inset: SAED patterns of individual nanorod and enlarged high-resolution TEM image. The EDS pattern of the individual (e) c-nanorod and (f) m-nanorod.[79,80]

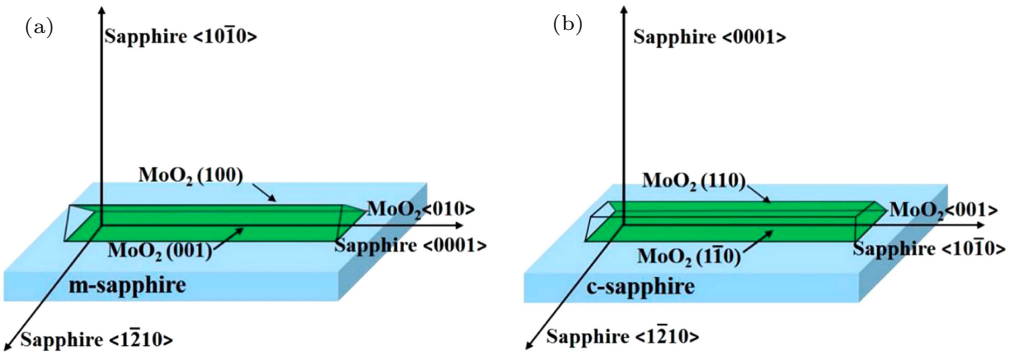


Fig. 6. Three-dimension growth models of (a) m-nanorod and (b) c-nanorod.[80]

We draw the following conclusions: m-nanorods grow along the sapphire ⟨0001⟩ with the two sides being MoO_2(100) and (001), as the model shown in Fig. 6(a); c-nanorods grow along the sapphire ⟨$10\bar{1}0$⟩ with the two sides being MoO_2 (110) and ($1\bar{1}0$), as the model shown in Fig. 6(b).

The electrical measurements of devices based on individual transferred m- and c-nanorods were made, comparatively. Devices with multiple electrodes were fabricated using e-beam lithography (EBL).[118] The inset in Fig. 7(a) displays the SEM image of a c-nanorod based device with four electrodes. The electric resistance (R) between electrodes 2 and 3 was measured to be 45 Ω. The electric conductivity is calculated to be 6.04×10^3 S/cm, which is significantly higher than previously reported values.[111,112] The corresponding temperature-dependent I–V curves as shown in Fig. 7(b) reveal the metallic nature, as the resistance decreases along with temperature.

The contact resistance was calculated to be $\sim 33\ \Omega$, shown in Fig. 7(c), which is three orders of magnitude less than previous reported values.[112] For m-nanorods, the I–V curve shown in Fig. 7(d) is almost linear. According to Ohm's law,[119] the conductivity is calculated to be only ~ 59 S/cm.

All the results demonstrate the metallic nature of the MoO_2 nanorods and their high degree of crystallinity.[120] The disparity between c- and m-nanorods demonstrates that the crystallographic directions of nanorods have a great influence on conductivity.[121] However, the effect of substrates and measurement method could not be rule out. These metallic MoO_2 nanorods are good candidates for use as electrical transport materials at low electric fields.[122]

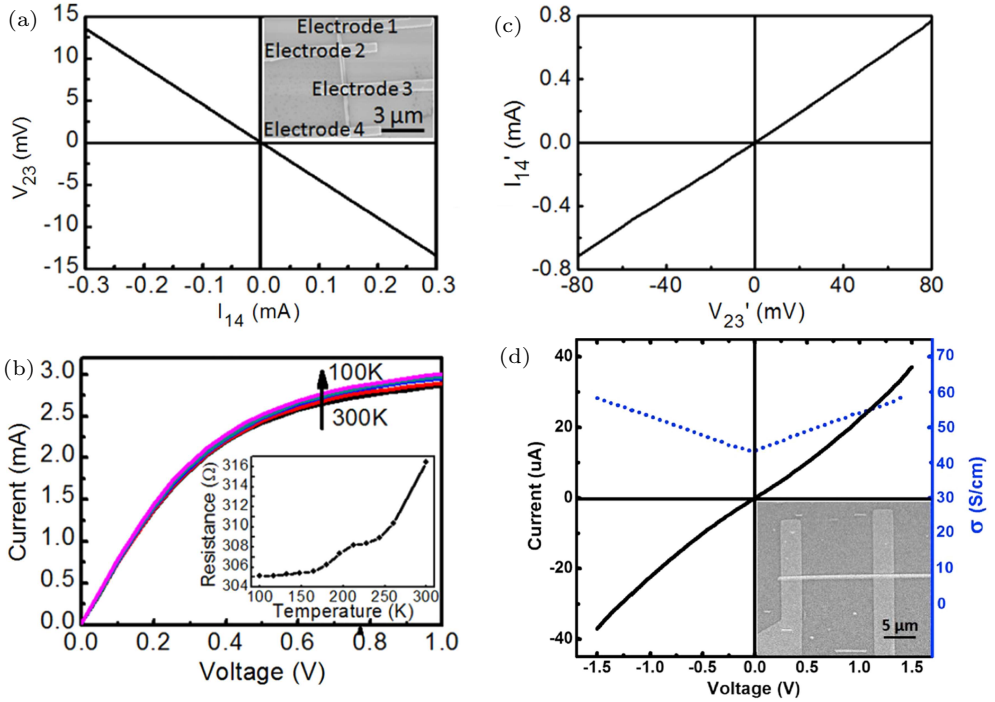


Fig. 7. Electrical properties. (a) V_{23}–I_{14} curve of individual c-nanorod. Inset: SEM image of the device. (b) I–V characteristics measured as a function of the ambient temperature. Inset: Resistance of the channel versus ambient temperature. (c) I_{14} as a function of V_{23}. (d) I–V curve (solid black line) and conductivity curve (dotted blue line) of individual m-nanorod. Inset: The SEM image of the device.[80,81]

Based on MoO_2@MoS_2 core–shell nanorods obtained, we report a facile approach to prepare single- and bi-layered MoS_2 nanoribbons by PMMA assisted decoupling, as schematically shown in Fig. 8(a). Interestingly, it is found that only MoS_2 was transferred. Figure 8(b) shows a typical AFM topography image of the transferred MoS_2 nanoribbon. The inserted height profile in Fig. 8(b) reveals that the transferred MoS_2 nanoribbon is bilayer.

It is well known that the PL quantum yield of MoS_2 decreases with the increasing number of layers.[123,124] Figure 8(c) shows the PL spectrum of triangle-shaped c-MoS_2, c-MoO_2@MoS_2 nanorod, and transferred MoS_2 nanoribbon with reasonable fitting. The comparable PL intensities for MoS_2 flake and MoO_2@MoS_2 nanorod reveal their monolayer nature. The PL spectrum of triangle-shaped c-MoS_2 shows the highest intensity and consists of three components at 1.83 eV (A^-), 1.86 eV (A), and 1.98 eV (B). The disappearance of the B peak for the middle spectrum can be attributed to the metallic nature of the MoO_2 core. This confirms the high quality and single layer nature of the MoS_2-shell. The PL spectrum of the folded MoS_2 nanoribbon on SiO_2/Si substrate is much weaker and consists of three components at 1.78 eV, 1.84 eV, and 1.96 eV, where the much enhanced intensity of the B peak may attribute to the increased strain after transfer, confirming the bilayer nature, in consistence with the above AFM results.

Figure 8(d) presents the schematic representation of the formation process of a MoS_2 nanoribbon from a staple-like MoS_2-shell. During the PMMA removal process, there are a few kinds of forces acting on MoS_2-shell, the adhesion between MoS_2 and substrate (F_1), the tension between MoS_2 and acetone droplets (F_2), as well as the tension between MoS_2 and PMMA (F_3). The competition among them will result in both sides of MoS_2-shell bending to opposite directions, like a staple, inward or outward, as shown in step 2. The necked-in MoS_2-shell continues bending to form the folded bi-layer nanoribbon under the vdW interactions between layers (F_4), while the necked-out one to form flat single layer nanoribbon under F_1. The folded bilayer MoS_2 nanoribbons have a half width and twice height relative to single-layered ones. The corresponding PL intensity is quenched due to interlayer coupling. All the conclusions agree well with previous experimental results. No scrolling can be attributed to the high stiffness of single-layer MoS_2.

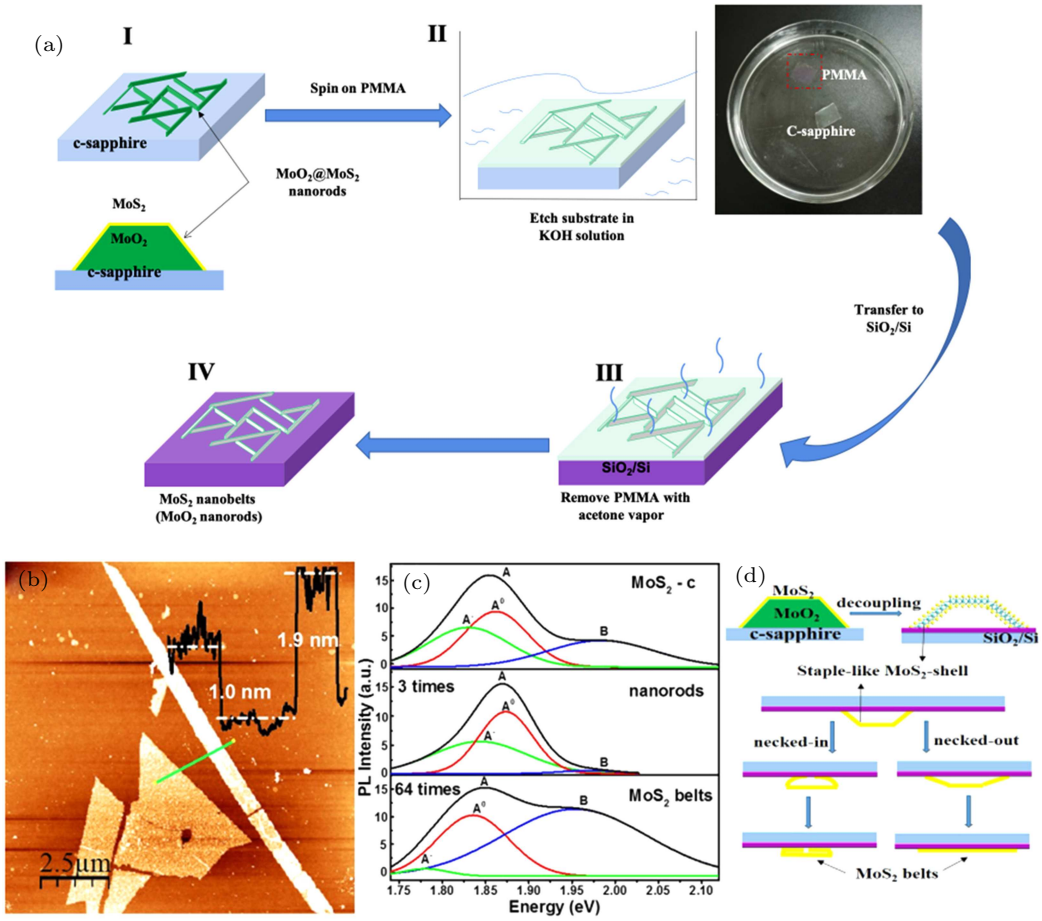


Fig. 8. MoS_2 nanoribbons by PMMA assisted decoupling. (a) Schematic diagram of the proposed transfer progress. (b) AFM topography of transferred MoS_2 flake and nanoribbon. Inset: Height profiles of line scans marked in (b). (c) PL spectra of the MoS_2 flake, MoO_2@MoS_2 nanorod, and transferred MoS_2 nanoribbon. (d) Schematic representation of the formation of MoS_2 nanoribbons on SiO_2/Si.[82]

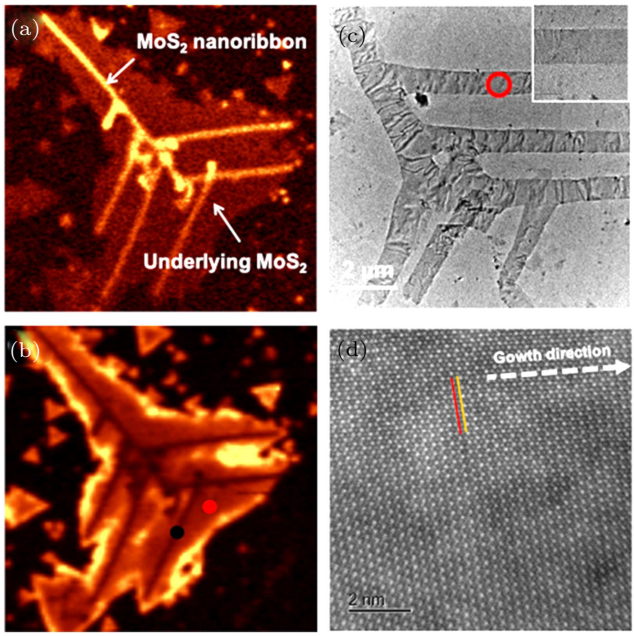


Fig. 9. CVD grown MoS_2 nanoribbons without catalysts. (a) The Raman E^1_{2g} and (b) PL A intensity maps of MoS_2 nanoribbons. (c) Low magnification TEM image of transferred MoS_2 nanoribbons. (d) ADF-STEM image of MoS_2 nanoribbons in the [0001] zone.[83]

The 1D MoS_2 nanoribbons can be fabricated via CVD method without catalysts. Figures 9(a) and 9(b) show the representative Raman E^1_{2g} and PL A^0 intensity images of MoS_2 nanoribbons. The intensity contrast in each image is consistent with the spectra results. The homogenous contrast in nanoribbons and bottom flakes area indicates that the MoS_2 possesses a uniform crystalline degree in the whole sample. Figure 9(c) shows a low magnification TEM image of a branch of MoS_2 nanoribbons. The inset displays a close-up of one nanoribbon, exhibiting straight and sharp edges. Figure 9(d) displays the annular dark field STEM image of MoS_2 nanoribbons marked in Fig. 9(c). The orientation from top to bottom is almost perpendicular to the growth direction. The growth facet of such nanoribbons is Mo-zigzag edge termination. These findings offer insights into the synthesis of various TMDC 1D structures and the potential applications in the field of catalysis.

3. 2D TMOs/TMDCs heterojunction

2D MX_2, such as MoS_2, WSe_2, and $MoSe_2$ possess special layer-depended electronic and optical properties.[125–128] For example, WSe_2 possess thickness-depended carrier types: p-type (< 4 nm), ambipolar (≈ 6 nm), and n-type (> 15 nm).[75] One of the unique optical properties of MX_2 is the indirect-to-direct band gap transition when the thickness is changed from bulk to a monolayer. Controllable reducing

the thickness becomes a novel method to tune their properties, including laser thinning, thermal etching, etc.[129–131] Following, the controlled layer-by-layer oxidation of MoX_2 via UVO, a convenient and effective method, is demonstrated to control the MoX_2 thickness and to enormously enhance the electrical and optoelectronic properties of MoX_2.

Figure 10(a) presents the selected Raman spectra of tetralayer $MoTe_2$ flakes upon intermittent UVO treatment for 0, 2 min, 6 min, 20 min, 50 min. For the few-layer $MoTe_2$ crystals, three distinctive Raman modes can be observed, the in-plane E^1_{2g} mode ($\sim$ 232 cm^{-1}), the out-of plane A_{1g} mode ($\sim$ 171 cm^{-1}), and the bulk in-active B^1_{2g} phonon mode ($\sim$288 cm^{-1}). The increasing in intensity of B^1_{2g} as shown in Fig. 10(a) indicates that the $MoTe_2$ flakes are thinned upon UVO treatment.[132,133] After oxidation for 2 min, monolayer $MoTe_2$ shows neither E^1_{2g} or B^1_{2g} mode, whereas bilayer $MoTe_2$ exhibits only the E^1_{2g} mode. This implies that the topmost layer is oxidized into a homogeneous atomically flat oxide film of MoO_x. Additional 4 min exposure leads to the vanish of the B^1_{2g} mode in trilayer not the tetralayer $MoTe_2$ flakes, i.e., the top two layers are oxidized. The mode B^1_{2g} varies significantly and systematically upon the number of layers varying. The intensity ratio of B^1_{2g}/E^1_{2g} [Fig. 10(a) inset] being 0.34 and 0 can be used as an good index to estimate whether a few-layer $MoTe_2$ has been thinned down to bilayer and monolayer. The tetralayer flake is thinned down to bilayer and monolayer upon 6 min and 20 min exposure, respectively. The corresponding E^1_{2g} and B^1_{2g} modes mapping shown in Fig. 10(b) reveals the homogeneous oxidation process. AFM images of a 5-layered $MoTe_2$ flake before and after 100 min UVO treatment reveal that the MoX_2 thickness increases by 1.6 nm owing to the formation of amorphous oxides MoO_x. However, the MoO_x layer shows a smooth and uniform surface morphology with a root-mean-square roughness about 0.29 nm, similar to that of pristine $MoTe_2$, implying the compactness of newly-formed MoO_x. Depending on the oxidation time, the layer number of $MoTe_2$ and the thickness of MoO_x can be tuned.

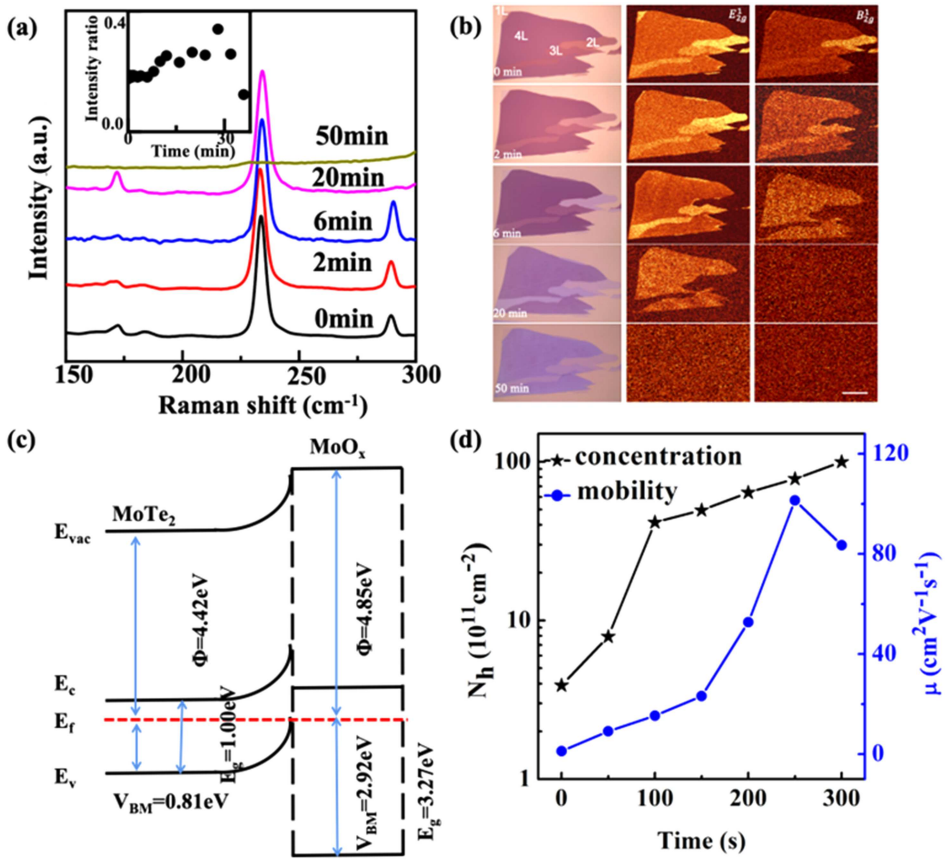


Fig. 10. Layer-by-layer oxidation of few-layer $MoTe_2$ using UVO. (a) Raman spectra (laser wavelength 532 nm) of tetralayer $MoTe_2$ upon intermittent UVO exposure from 0 to 50 min. The inset shows the intensity ratio of B^1_{2g}/E^1_{2g}. (b) The corresponding Raman mapping of B^1_{2g} and E^1_{2g} modes. The scale bar is 5 μm. (c) Extracted parameters as a function of UVO treatment time: mobility μ (left axis) and hole concentration n_h (right axis) in logarithmic coordinates. (d) The corresponding band diagram.[84,86]

It is well-known that MoO_x is a famous p-type dopant. Our photoemission investigations reveal the band diagram at the interface between $MoTe_2$ and MoO_x as shown in Fig. 10(c). By forming MoO_x on top of $MoTe_2$, the large WF difference between MoO_x (4.85 eV) and $MoTe_2$ (4.42 eV) could drive the spontaneous electron transfer from $MoTe_2$ to MoO_x, facilitating the formation of a hole accumulation layer in $MoTe_2$, resulting in effective hole doping. The effect of

the formation of MoO_x on the transport properties of an 8-layer $MoTe_2$ based FETs is studied, as shown in Fig. 10(d). The calculated hole mobility (μ_h) of UVO treated $MoTe_2$ increases by nearly 2 orders of magnitude compared to the pristine one. This value is substantially higher than previous reported one. However, the μ_h reduced when the treatment time increased from 250 s to 300 s (Fig. 10(d)), which can be attributed to that the hole–hole scattering increases with concentration. Higher hole concentration induced degenerate doping appears after 250 s UVO treatment. Time dependent electrical performance testing in air reveals the good air stability of MoO_x-doped $MoTe_2$ device.

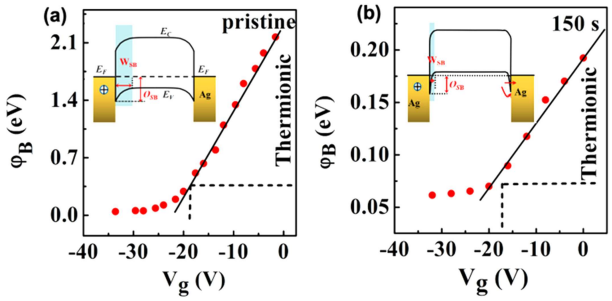


Fig. 11. (a)–(b) Extracted effective barrier height φ_B of pristine and UVO treatment $MoTe_2$ FETs as a function of V_g. Insets in panels (a) and (b): Energy band structures between metal contacts and $MoTe_2$ before and after MoO_x doping. E_F is the Fermi level energy. E_C and E_V represent the minimum energy of conduction band and the maximum energy of valance band, respectively. Φ_{SB} and W_{SB} are the Schottky barrier height and width, respectively. The Schottky barrier formed at metal/$MoTe_2$ interface is compressed for hole doped $MoTe_2$ device, facilitating the tunneling transport of hole. [86]

MoO_x induced surface charge transfer doping can also improve the electrical and photoelectric properties of MX_2. According to the thermionic emission model,[134] the current through a Schottky barrier can be characterized with $I_d = AT^{3/2}\exp(-q\Phi_{SB}/k_BT)[1-\exp(-qV_d/k_BT)]$, where A is the Richardson constant, T is the temperature, Φ_{SB} is the Schottky barrier height, and k_B is the Boltzmann constant. Φ_{SB} of $MoTe_2$ before and after 150 s UVO treatment can be extracted from temperature dependent I_d–V_g curves, as shown in the Arrhenius plots in Figs. 11(a) and 11(b). The φ_B in Y-axis is the total activation energy that causes the hole into the $MoTe_2$ channel from electrode for each V_g. It decreases linearly with deceasing V_g in the case that thermionic emission dominates the current flow, while it deviates from the linear trend in the case that tunneling dominates. At the intersection, the φ_B corresponds to Φ_{SB}. The extracted Φ_{SB} of UVO treated $MoTe_2$ (60 meV) is lower than that of pristine one (400 meV), attributed to the regulation of the band alignment by MoO_x doping. P-type doping induces the E_F of $MoTe_2$ moving downwards to its valence band, as seen in the change of band diagram in the corresponding insets. Thus, the electrical performance is much enhanced. For example, the $MoTe_2$ after doping shows high mobility 83.5 $cm^{-2}\cdot V^{-1}\cdot s^{-1}$ and on-current 54 μA at $V_d = 1$ V.

The corresponding Schottky barrier width (W_{SB}) is also estimated according to the following model:[135,136]

$$W_{SB} = \sqrt{\frac{2\varepsilon_s}{qn}\left(\varphi_{bi} - V_{ds} - \frac{kT}{q}\right)}, \tag{1}$$

where ε_s is the dielectric constant, q is the electron charge, V_{ds} is the bias, T is the temperature, N is the semiconductor doping concentration, and φ_{bi} is the built-in potential between the semiconductor and metal electrode.

The φ_{bi} decreases because of the decreased Φ_{SB}. n_h is enhanced due to surface charge transfer doping. Therefore, the W_{SB} is compressed and the current through the metal–semiconductor contact is greatly enhanced. These lead to the formation of quasi-ohmic contact, which has been clearly proved by the evolution of gate-dependent I_d–V_d curves and the greatly reduced contact resistance.

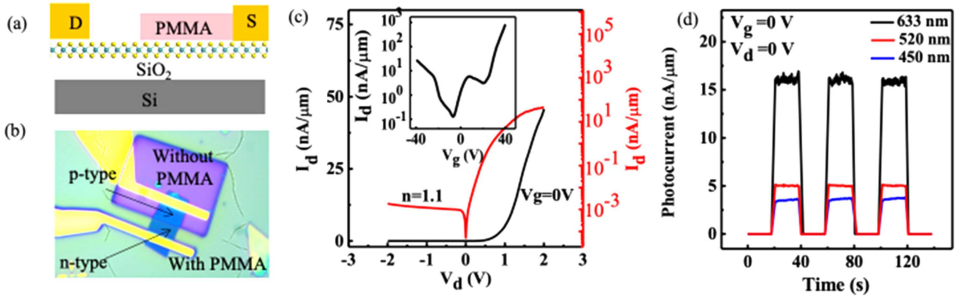


Fig. 12. Lateral $MoSe_2$ p–n junction. (a) The cross section schematic structure of the lateral p–n junction device. (b) The optical photograph of p–n device. (c) I_d–V_d curve of the $MoSe_2$ diode in linear (black line) and log (red) scale at $V_g = 0$ V. The inset shows the transfer characteristic I_d–V_g curve of the $MoSe_2$ diode at $V_d = 1$ V. (d) Dynamic optical response of the device ($V_d = 0$ V, $V_g = 0$ V) under illumination of light of 450 nm, 520 nm, 633 nm.[85]

This method can be used to tune intrinsic n-type few-layer $MoSe_2$ to p-type. As shown in Figs. 12(a) and 12(b), local p–n homojunction diode was fabricated upon 10 min UVO treatment on EBL partially patterned few layer $MoSe_2$ transistor. Figure 12(c) shows the corresponding I_d–V_d curves with $V_g = 0$ V in the linear (black line) and log (red) scale. A superior rectification ratio (RR) of 2.4×10^4 and an ideality factor of 1.1 demonstrate the good performance of the p–n junc-

tion. The corresponding transfer characteristics inserted in Fig. 12(c) with two current minimums (at ~ 7 V and ~ +21 V) confirms the successful preparation of p–n junction.[137] As shown in Fig. 12(d), the photoresponsivity (R) of the p–n junction to 633 nm laser is about 20 times higher than that of the previous reported monolayer $MoSe_2$ photoconductor and comparable to that of the $MoSe_2$–MoO_x heterojunction device.[138]

4. Conclusion & outlook

MoO_x as promising materials with low evaporation temperature, high WF up to 6.3 eV, and inertness to air have been widely used in the fabrication and modification of TMDCs. In summary, except for large-scale high-quality single-crystal monolayer MoS_2 flakes, 1D MoO_2 and MoO_2@MoS_2 nanorods with varied crystalline directions as well as 1D MoS_2 nanoribbons with atomic sharp edges can be synthesized via APCVD method on different sapphire substrates. This provides one way to further tune the properties of TMDCs. On the other hand, few-layered MoX_2 can be oxidized into dense MoO_x in a layer-by-layer mode via UVO exposure. The formed MoO_x can protect the underlying MoX_2 from air and result in p-doping of them via a surface charge transfer doping mechanism and in improvement of their electrical and photoelectrical properties via reduction of Schottky barriers. Our findings provide two classes of ways to tune the properties of 2D TMDCs and are common to other TMOs and TMDCs. In the next step, the mechanisms need to be explored accurately at the atomic scale in order to learn the possible interaction between TMOs and TMDCs, which are beneficial for improving their performance.

References

[1] Allen M J, Tung V C and Kaner R B 2010 *Chem. Rev.* **110** 132
[2] Kim K, Choi J Y, Kim T, Cho S H and Chung H J 2011 *Nature* **479** 338
[3] Tan C, Cao X, Wu X J, He Q, Yang J, Zhang X, Chen J, Zhao W, Han S, Nam G H, Sindoro M and Zhang H 2017 *Chem. Rev.* **117** 6225
[4] Xu M, Liang T, Shi M and Chen H 2013 *Chem. Rev.* **113** 3766
[5] Wang Q H, Kalantar-Zadeh K, Kis A, Coleman J N and Strano M S 2012 *Nat. Nanotechnol.* **7** 699
[6] Luo F, Fan Y, Peng G, Xu S, Yang Y, Yuan K, Liu J, Ma W, Xu W and Zhu Z H 2019 *ACS Photonics* **6** 2117
[7] Geim A K 2009 *Science* **324** 1530
[8] Novoselov K S, Jiang D, Schedin F, Booth T, Khotkevich V, Morozov S and Geim A K 2005 *Proc. Natl. Acad. Sci. USA* **102** 10451
[9] Jo I, Pettes M T, Kim J, Watanabe K, Taniguchi T, Yao Z and Shi L 2013 *Nano Lett.* **13** 550
[10] Akinwande D, Petrone N and Hone J 2014 *Nat. Commun.* **5** 3586
[11] Manzeli S, Ovchinnikov D, Pasquier D, Yazyev O V and Kis A 2017 *Nat. Rev. Mater.* **2** 17033
[12] Jariwala D, Sangwan V K, Lauhon L J, Marks T J and Hersam M C 2014 *ACS Nano* **8** 1102
[13] Koenig S P, Doganov R A, Schmidt H, Castro Neto A and Özyilmaz B 2014 *Appl. Phys. Lett.* **104** 103106
[14] Castellanos-Gomez A, Vicarelli L, Prada E, Island J O, Narasimha-Acharya K, Blanter S I, Groenendijk D J, Buscema M, Steele G A and Alvarez J 2014 *2D Mater.* **1** 025001
[15] Liu H, Du Y, Deng Y and Peide D Y 2015 *Chem. Soc. Rev.* **44** 2732
[16] Drummond N, Zolyomi V and Fal'Ko V 2012 *Phys. Rev. B* **85** 075423
[17] Tao L, Cinquanta E, Chiappe D, Grazianetti C, Fanciulli M, Dubey M, Molle A and Akinwande D 2015 *Nat. Nanotechnol.* **10** 227
[18] Ni Z, Liu Q, Tang K, Zheng J, Zhou J, Qin R, Gao Z, Yu D and Lu J 2012 *Nano Lett.* **12** 113
[19] Dávila M, Xian L, Cahangirov S, Rubio A and Le Lay G 2014 *New J. Phys.* **16** 095002
[20] Wang H, Yu L, Lee Y H, Shi Y, Hsu A, Chin M L, Li L J, Dubey M, Kong J and Palacios T 2012 *Nano Lett.* **12** 4674
[21] Liu G B, Xiao D, Yao Y, Xu X and Yao W 2015 *Chem. Soc. Rev.* **44** 2643
[22] Jiang J, Hu W, Xie D, Yang J, He J, Gao Y and Wan Q 2019 *Nanoscale* **11** 1360
[23] Ji Q, Zhang Y, Zhang Y and Liu Z 2015 *Chem. Soc. Rev.* **44** 2587
[24] Pu J, Yomogida Y, Liu K K, Li L J, Iwasa Y and Takenobu T 2012 *Nano Lett.* **12** 4013
[25] Yin Z, Li H, Li H, Jiang L, Shi Y, Sun Y, Lu G, Zhang Q, Chen X and Zhang H 2011 *ACS Nano* **6** 74
[26] Zhang W, Huang J K, Chen C H, Chang Y H, Cheng Y J and Li L J 2013 *Adv. Mater.* **25** 3456
[27] Roy K, Padmanabhan M, Goswami S, Sai T P, Ramalingam G, Raghavan S and Ghosh A 2013 *Nat. Nanotechnol.* **8** 826
[28] Yu L, Lee Y H, Ling X, Santos E J, Shin Y C, Lin Y, Dubey M, Kaxiras E, Kong J and Wang H 2014 *Nano Lett.* **14** 3055
[29] Lee G H, Yu Y J, Cui X, Petrone N, Lee C H, Choi M S, Lee D Y, Lee C, Yoo W J and Watanabe K 2013 *ACS Nano* **7** 7931
[30] Baugher B W, Churchill H O, Yang Y and Jarillo-Herrero P 2013 *Nano Lett.* **13** 4212
[31] Schmidt H, Wang S, Chu L, Toh M, Kumar R, Zhao W, Neto A H, Martin J, Adam S, Özyilmaz B and Eda G 2014 *Nano Lett.* **14** 1909
[32] Han W, Liu K, Yang S, Wang F, Su J, Jin B, Li H and Zhai T 2019 *Sci. China Chem.* **62** 1300
[33] Cai Z, Liu B, Zou X and Cheng H-M 2018 *Chem. Rev.* **118** 6091
[34] Wang Q, Lei Y, Wang Y, Liu Y, Song C, Zeng J, Song Y, Duan X, Wang D and Li Y 2020 *Energy Environ. Sci.* **13** 1593
[35] Fang L, Chen H, Yuan X, Huang H, Chen G, Li L, Ding J, He J and Tao S 2019 *Nanoscale Res. Lett.* **14** 274
[36] Jiang J, Li N, Zou J, Zhou X, Eda G, Zhang Q, Zhang H, Li L-J, Zhai T and Wee A T 2019 *Chem. Soc. Rev.* **48** 4639
[37] Fang L, Yuan X, Liu K, Li L, Zhou P, Ma W, Huang H, He J and Tao S 2020 *Nanoscale* **12** 3715
[38] Dong R, Zhang T and Feng X 2018 *Chem. Rev.* **118** 6189
[39] Zhou J, Lin J, Huang X, Zhou Y, Chen Y, Xia J, Wang H, Xie Y, Yu H and Lei J 2018 *Nature* **556** 355
[40] Kang K, Xie S, Huang L, Han Y, Huang P Y, Mak K F, Kim C J, Muller D and Park J 2015 *Nature* **520** 656
[41] Tongay S, Fan W, Kang J, Park J, Koldemir U, Suh J, Narang D S, Liu K, Ji J and Li J 2014 *Nano Lett.* **14** 3185
[42] Gong Y, Lei S, Ye G, Li B, He Y, Keyshar K, Zhang X, Wang Q, Lou J and Liu Z 2015 *Nano Lett.* **15** 6135
[43] Ouyang F, Yang Z, Ni X, Wu N, Chen Y and Xiong X 2014 *Appl. Phys. Lett.* **104** 071901
[44] Kosynkin D V, Higginbotham A L, Sinitskii A, Lomeda J R, Dimiev A, Price B K and Tour J M 2009 *Nature* **458** 872
[45] Jiao L, Zhang L, Wang X, Diankov G and Dai H 2009 *Nature* **458** 877
[46] Li S, Lin Y C, Zhao W, Wu J, Wang Z, Hu Z, Shen Y, Tang D M, Wang J and Zhang Q 2018 *Nat. Mater.* **17** 535
[47] Zhou D, Li H, Si N, Jiang Y, Huang H, Li H and Niu T 2020 *Appl. Phys. Lett.* **116** 061602
[48] Chen Y, Sun J, Qiu W, Wang X, Liu W, Huang Y, Dai G, Yang J and Gao Y 2019 *Appl. Phys. A* **125** 691
[49] Kang L, Chen H, Yang Z J, Yuan Y, Huang H, Yang B, Gao Y and Zhou C 2018 *J. Appl. Phys.* **123** 205110
[50] Li X, Wang X, Zhang L, Lee S and Dai H 2008 *Science* **319** 1229
[51] Terrones M 2009 *Nature* **458** 845
[52] Cai J, Ruffieux P, Jaafar R, Bieri M, Braun T, Blankenburg S, Muoth M, Seitsonen A P, Saleh M and Feng X 2010 *Nature* **466** 470
[53] Ruffieux P, Wang S, Yang B, Sánchez-Sánchez C, Liu J, Dienel T, Talirz L, Shinde P, Pignedoli C A and Passerone D 2016 *Nature* **531** 489
[54] Tian G, Shen Y, He B, Yu Z, Song F, Lu Y, Wang P, Gao Y and Huang H 2017 *Surf. Sci.* **665** 89
[55] He B, Tian G, Gou J, Liu B, Shen K, Tian Q, Yu Z, Song F, Xie H and Gao Y 2019 *Surf. Sci.* **679** 147
[56] Tian Q, He B, Zhao Y, Wang S, Xiao J, Song F, Wang Y, Lu Y, Xie H and Huang H 2019 *Synth. Met.* **251** 24
[57] Xu G, Wang X, Sun Y, Chen X, Zheng J, Sun L, Jiao L and Li J 2015 *Nano Res.* **8** 2946

[58] Botello-Méndez A R, Lopez-Urias F, Terrones M and Terrones H 2009 *Nanotechnology* **20** 325703
[59] Cai Y, Zhang G and Zhang Y W 2014 *J. Am. Chem. Soc.* **136** 6269
[60] Mak K F, He K, Shan J and Heinz T F 2012 *Nat. Nanotechnol.* **7** 494
[61] Meyer J, Kidambi P R, Bayer B C, Weijtens C, Kuhn A, Centeno A, Pesquera A, Zurutuza A, Robertson J and Hofmann S 2014 *Sci. Rep.* **4** 5380
[62] Huang J, Xu Z and Yang Y 2007 *Adv. Funct. Mater.* **17** 1966
[63] Lin J D, Han C, Wang F, Wang R, Xiang D, Qin S, Zhang X-A, Wang L, Zhang H and Wee A T S 2014 *ACS Nano* **8** 5323
[64] Lei B, Hu Z, Xiang D, Wang J, Eda G, Han C and Chen W 2017 *Nano Res.* **10** 1282
[65] Xiang D, Han C, Wu J, Zhong S, Liu Y, Lin J, Zhang X A, Hu W P, Ozyilmaz B and Neto A C 2015 *Nat. Commun.* **6** 6485
[66] Lou Y H, Xu M F, Zhang L, Wang Z K, Naka S, Okada H and Liao L S 2013 *Org. Electron.* **14** 2698
[67] Gwinner M C, Pietro R D, Vaynzof Y, Greenberg K J, Ho P K, Friend R H and Sirringhaus H 2011 *Adv. Funct. Mater.* **21** 1432
[68] Liu X, Wang C, Yi S and Gao Y 2014 *Org. Electron.* **15** 977
[69] Zhang M, Irfan, Ding H, Gao Y and Tang C W 2010 *Appl. Phys. Lett.* **96** 183301
[70] Wang C, Irfan I and Gao Y 2014 *Appl. Phys. Lett.* **105** 181602
[71] Gao Y 2010 *Mater. Sci. Eng. R Rep.* **68** 39
[72] Wang C, Irfan I, Liu X and Gao Y 2014 *J. Vac. Sci. Technol. B* **32** 040801
[73] Irfan I, James Turinske A, Bao Z and Gao Y 2012 *Appl. Phys. Lett.* **101** 093305
[74] Choi S, Fuentes-Hernandez C, Wang C-Y, Khan T M, Larrain F A, Zhang Y, Barlow S, Marder S R and Kippelen B 2016 *ACS Appl. Mater. Interfaces* **8** 24744
[75] Zhou C, Zhao Y, Raju S, Wang Y, Lin Z, Chan M and Chai Y 2016 *Adv. Funct. Mater.* **26** 4223
[76] Meyer J, Hamwi S, Kröger M, Kowalsky W, Riedl T and Kahn A 2012 *Adv. Mater.* **24** 5408
[77] Ho P H, Chang Y R, Chu Y C, Li M K, Tsai C A, Wang W H, Ho C H, Chen C W and Chiu P W 2017 *ACS Nano* **11** 7362
[78] Yamamoto M, Dutta S, Aikawa S, Nakaharai S, Wakabayashi K, Fuhrer M S, Ueno K and Tsukagoshi K 2015 *Nano Lett.* **15** 2067
[79] Wu D, Yang Y, Zhu P, Zheng X, Chen X, Shi J, Song F, Gao X, Zhang X, Ouyang F, Xiong X, Gao Y and Huang H 2018 *J. Phys. Chem. C* **122** 1860
[80] Liu J, Shi J, Wu D, Zheng X, Chen F, Xiao J, Li Y, Song F, Gao Y and Huang H 2020 *Curr. Appl. Phys.* **20** 1130
[81] Xie Q, Zheng X, Wu D, Chen X, Shi J, Han X, Zhang X, Peng G, Gao Y and Huang H 2017 *Appl. Phys. Lett.* **111** 093505
[82] Shi J, Wu D, Zheng X, Xie D, Song F, Zhang X, Jiang J, Yuan X, Gao Y and Huang H 2018 *Phys. Status Solidi (B)* **255** 1800254
[83] Wu D, Shi J, Zheng X, Liu J, Dou W, Gao Y, Yuan X, Ouyang F and Huang H 2019 *Phys Status Solidi Rapid Res Lett* **13** 1900063
[84] Zheng X, Wei Y, Deng C, Huang H, Yu Y, Wang G, Peng G, Zhu Z, Zhang Y, Jiang T, Qin S, Zhang R and Zhang X 2018 *ACS Appl. Mater. Interfaces* **10** 30045
[85] Zheng X, Wei Y, Liu J, Wang S, Shi J, Yang H, Peng G, Deng C, Luo W, Zhao Y, Li Y, Sun K, Wan W, Xie H, Gao Y, Zhang X and Huang H 2019 *Nanoscale* **11** 13469
[86] Zheng X, Zhang X, Wei Y, Liu J, Yang H, Zhang X, Wang S, Xie H, Deng C and Gao Y 2020 *Nano Res.* **13** 952
[87] Xie H, Huang H, Cao N, Zhou C, Niu D and Gao Y 2015 *Physica B* **477** 14
[88] Sun H, Liang Z, Shen K, Hu J, Ji G, Li Z, Li H, Zhu Z, Li J and Gao X 2017 *Surf. Sci.* **661** 34
[89] Kumar P, Singh M, Sharma R K and Reddy G 2016 *Mater. Res. Express* **3** 055021
[90] Kumar P, Singh M and Reddy G 2017 *Mater. Res. Express* **4** 036405
[91] Qian F, Gradecak S, Li Y, Wen C-Y and Lieber C M 2005 *Nano Lett.* **5** 2287
[92] Mariani G, Zhou Z, Scofield A and Huffaker D L 2013 *Nano Lett.* **13** 1632
[93] Chen G, Ågren H, Ohulchanskyy T Y and Prasad P N 2015 *Chem. Soc. Rev.* **44** 1680
[94] Zheng L, Xu Y, Jin D and Xie Y 2010 *J. Mater. Chem.* **20** 7135
[95] Liu J, Zhang Z, Pan C, Zhao Y, Su X, Zhou Y and Yu D 2004 *Mater. Lett.* **58** 3812
[96] Vorobeva N S, Lipatov A, Muratov D S and Sinitskii A 2018 *Nanotechnology* **29** 505707
[97] Ma Y R, Tsai C C, Lee S F, Cheng K W, Liou Y and Der Yao Y 2006 *J. Magn. Magn. Mater.* **304** e13
[98] Yang T H, Aggarwal R, Gupta A, Zhou H, Narayan R J and Narayan J 2010 *J. Appl. Phys.* **107** 053514
[99] Zhang F, Saito K, Tanaka T, Nishio M and Guo Q 2014 *J. Cryst. Growth* **387** 96
[100] Zhao Y, Hwan Lee J, Zhu Y, Nazari M, Chen C, Wang H, Bernussi A, Holtz M and Fan Z 2012 *J. Appl. Phys.* **111** 053533
[101] Baker T J, Haskell B A, Wu F, Speck J S and Nakamura S 2006 *Jpn. J. Appl. Phys.* **45** L154
[102] Scheuschner N, Gillen R, Staiger M and Maultzsch J 2015 *Phys. Rev. B* **91** 235409
[103] Wang S, Rong Y, Fan Y, Pacios M, Bhaskaran H, He K and Warner J H 2014 *Chem. Mater.* **26** 6371
[104] Hao S, Yang B and Gao Y 2017 *Physica Status Solidi (B)* **254** 1600245
[105] Kumari L, Ma Y R, Tsai C C, Lin Y W, Wu S Y, Cheng K W and Liou Y 2007 *Nanotechnology* **18** 115717
[106] Spevack P and McIntyre N 1992 *J. Phys. Chem.* **96** 9029
[107] Dieterle M, Weinberg G and Mestl G 2002 *Phys. Chem. Chem. Phys.* **4** 812
[108] Wang X, Feng H, Wu Y and Jiao L 2013 *J. Am. Chem. Soc.* **135** 5304
[109] Mukundan S, Mohan L, Chandan G, Roul B and Krupanidhi S 2014 *J. Appl. Phys.* **116** 204502
[110] Pu E, Liu D, Ren P, Zhou W, Tang D, Xiang B, Wang Y and Miao J 2017 *AIP Adv.* **7** 025015
[111] Bhosle V, Tiwari A and Narayan J 2005 *J. Appl. Phys.* **97** 083539
[112] Hu B, Mai L, Chen W and Yang F 2009 *Acs Nano* **3** 478
[113] Ahn E, Seo Y S, Cho J, Lee I, Hwang J and Jeen H 2016 *RSC Adv.* **6** 60704
[114] Dahl-Petersen C, Šarić M, Brorson M, Moses P G, Rossmeisl J, Lauritsen J V and Helveg S 2018 *ACS Nano* **12** 5351
[115] Kumar P, Singh M, Sharma R K and Reddy G 2016 *Mater. Chem. Phys.* **178** 6
[116] Van Der Zande A M, Huang P Y, Chenet D A, Berkelbach T C, You Y, Lee G H, Heinz T F, Reichman D R, Muller D A and Hone J C 2013 *Nat. Mater.* **12** 554
[117] Li M Y, Shi Y, Cheng C C, Lu L S, Lin Y C, Tang H L, Tsai M L, Chu C W, Wei K H and He J H 2015 *Science* **349** 524
[118] Endo R, Maeda S, Jinnai Y, Lan R, Kuwahara M, Kobayashi Y and Susa M 2010 *Jpn. J. Appl. Phys.* **49** 065802
[119] Dai H, Rath A, Hearn Y S, Pennycook S J and Chua D H 2018 *J. Phys. Chem. Lett.* **9** 7185
[120] Ebbesen T, Lezec H, Hiura H, Bennett J, Ghaemi H and Thio T 1996 *Nature* **382** 54
[121] Ren X, Qi X, Shen Y, Xiao S, Xu G, Zhang Z, Huang Z and Zhong J 2016 *J Phy D: Appl Phys* **49** 315304
[122] Ayari A, Cobas E, Ogundadegbe O and Fuhrer M S 2007 *J. Appl. Phys.* **101** 014507
[123] Conley H J, Wang B, Ziegler J I, Haglund Jr R F, Pantelides S T and Bolotin K I 2013 *Nano Lett.* **13** 3626
[124] Mak K F, Lee C, Hone J, Shan J and Heinz T F 2010 *Phys. Rev. Lett.* **105** 136805
[125] Mak K F and Shan J 2016 *Nat. Photonics* **10** 216
[126] Eftekhari A 2017 *J. Mater. Chem. A* **5** 18299
[127] Yu Z L, Zhao Y Q, Liu B, Yang J L and Cai M Q 2020 *J. Phys. Condens. Matter* **32** 115703
[128] Qian M Y, Yu Z L, Wan Q, He P B, Liu B, Yang J L, Xu C M and Cai M Q 2020 *Phys. Status Solidi Rapid Res. Lett.* **14** 2000016
[129] Wu J, Li H, Yin Z, Li H, Liu J, Cao X, Zhang Q and Zhang H 2013 *Small* **9** 3314
[130] Das T, Seo D, Seo J E and Chang J 2020 *Adv. Electron. Mater.* **6** 2000008
[131] Hoffman A N, Gu Y, Tokash J, Woodward J, Xiao K and Rack P D 2020 *ACS Appl. Mater. Interfaces* **12** 7345
[132] Lezama I G, Arora A, Ubaldini A, Barreteau C, Giannini E, Potemski M and Morpurgo A F 2015 *Nano Lett.* **15** 2336
[133] Yamamoto M, Wang S T, Ni M, Lin Y F, Li S L, Aikawa S, Jian W B, Ueno K, Wakabayashi K and Tsukagoshi K 2014 *ACS Nano* **8** 3895
[134] Das S, Chen H Y, Penumatcha A V and Appenzeller J 2013 *Nano Lett.* **13** 100
[135] Liu J, Liu X, Chen Z, Liu Y and Li J 2019 *Nano Res.* **12** 463
[136] Sze S M and Ng K K 2006 *Physics of semiconductor devices* (John wiley & sons) p. 135
[137] Liu Y, Cai Y, Zhang G, Zhang Y W and Ang K W 2017 *Adv. Funct. Mater.* **27** 1604638
[138] Xia J, Huang X, Liu L Z, Wang M, Wang L, Huang B, Zhu D D, Li J J, Gu C Z and Meng X M 2014 *Nanoscale* **6** 8949